View Article Online
View Journal

Energy &
Environmental
Science

This article can be cited before page numbers have been issued, to do this please use: Q. Meng, Z. zhan, Y. Ma, Q. Qi, Y. Hua, Y. Yi, J. Yu, M. Wu, J. Tang, S. Cai, K. C. Chan and Z. Xu, *Energy Environ. Sci.*, 2026, DOI: 10.1039/D5EE07317K.

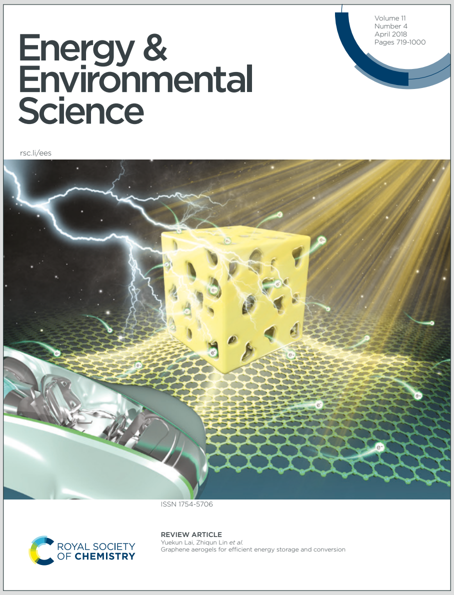

ROYAL SOCIETY
OF CHEMISTRY

rsc.li/ees

View Article Online
DOI: 10.1039/D5EE07317K

Broader context

With performance requirements constantly increasing on energy storage devices, there is much demand for highly affordable and high-energy density batteries that extend the capabilities of conventional lithium-ion systems. For the battery anodes, calcium (Ca) metal is considered to be one of the most attractive choices because of its negative electrochemical potential, exceptional nature abundance, and high theoretical capacities. However, reversible cycling Ca metal in aprotic organic electrolytes has been extremely difficult due to the anion-derived Ca ion-blocking passivation layers. Unlike the monovalent Li electrolytes, divalent Ca electrolytes exhibits stronger cation-anion coordination that promotes anion decomposition and the aggressive formation of inorganic-rich solid-electrolyte interphase (SEI). To address these fundamental challenges, this work introduces a two-pronged approach that decouples Ca ion-anion pairs in the bulky electrolyte and stabilizes the anion species to promote the formation of organic-rich SEI layers. The tailored interface supports fast Ca ion transport and enables Ca metal stripping/plating with low overpotentials. The anion-decoupling electrolyte design diverges conceptually from the widely explored anion-coupling paradigm for Li metal anodes, which offers a new mechanistic framework for advancing multivalent metal battery chemistries.

View Article Online
DOI: 10.1039/D5EE07317K

Anion-Decoupled Electrolytes Enable Stable Cycling and Fast Interfacial Kinetics for Calcium Metal Anodes

*Qi Meng, Zhen Zhan, Yiyuan Ma, Qi Qi, Yingkai Hua, Yuyang Yi, Jingya Yu, Mengcheng Wu, Jingjing Tang, Songhua Cai, Kang Cheung Chan, Zheng-Long Xu**

Qi Meng, Yiyuan Ma, Qi Qi, Yingkai Hua, Dr. Yuyang Yi, Dr. Jingya Yu, Mengcheng Wu, Prof. Kang Cheung Chan, Prof. Zheng-Long Xu

Department of Industrial and Systems Engineering, The Hong Kong Polytechnic University, Hung Hom, Hong Kong SAR, China.

E-mail: zhenglong.xu@polyu.edu.hk

Zhen Zhan, Prof. Songhua Cai

Department of Applied Physics, The Hong Kong Polytechnic University, Hung Hom, Hong Kong, China.

Prof. Kang Cheung Chan, Prof. Zheng-Long Xu

Research Institute for Advanced Manufacturing, The Hong Kong Polytechnic University, Hung Hom, Hong Kong SAR, China.

Prof. Zheng-Long Xu

Shenzhen Research Institute, The Hong Kong Polytechnic University, Shenzhen, China.

Prof. Jingjing Tang

School of Metallurgy and Environment, Central South University, Changsha, China.

View Article Online
DOI: 10.1039/D5EE07317K

Abstract

Calcium (Ca) metal battery is a promising post-lithium-ion technology due to the high energy density of Ca and its crustal abundance. However, the strong cation-anion interactions of divalent Ca^{2+} in conventional electrolytes promote the formation of Ca^{2+} ion-blocking solid electrolyte interphase (SEI) that hinders Ca metal electrodeposition. Here, we introduce an anion-decoupling strategy that combines a strongly coordinating solvent, dimethylacetamide (DMAc), with an anion-pulling 1,2-dibromobenzene (1,2-DBB) additive to regulate the widely accessible $Ca(TFSI)_2$-based electrolytes for reversible Ca metal anodes. Spectroscopic and theoretical analyses reveal that DMAc induces solvent-rich coordination structure and suppresses Ca^{2+}-$TFSI^-$ ion pairs, while 1,2-DBB further pulls $TFSI^-$ out of the primary solvation shell, hindering its decomposition into unfavorable CaF_2 in the SEI. The resulting inorganic-poor SEI enables fast Ca^{2+} transport and highly reversible Ca metal plating/stripping at low overpotentials of <0.19 V, compared to these of >5 V in conventional $Ca(TFSI)_2$ electrolytes. The optimized electrolyte supports stable cycling of Ca//Ca symmetric cells for over 340 hours and delivers >90% capacity retention over 200 cycles in Ca//graphite and Ca//9,10-phenanthrenequinone full cells. This work establishes anion-decoupling electrolyte chemistry, distinct from the well-established anion-coupling electrolyte chemistry for monovalent metal anodes (Li and Na), enabling fast interfacial kinetics and stable cycling of divalent metal anodes.

Keywords: anion-decoupling chemistry, multivalent-ion battery, fast kinetics, Ca metal anode

View Article Online
DOI: 10.1039/D5EE07317K

1. Introduction

Driven by the rapid expansion of the electrochemical energy storage market, post-lithium metal batteries have emerged as promising alternatives to current Li-ion batteries, owing to their potentially higher energy densities from metal anodes and better affordability from abundant elements.[1-3] Among the post-Li battery systems, calcium (Ca) metal batteries are particularly promising due to the low electrochemical potential (-2.87 V vs. standard hydrogen electrode), high theoretical capacities (1337 mAh g^{-1}, 2073 mAh cm^{-3}), excellent thermal stability (melting point: ~842°C), and the crustal abundance (ranking the 5th rich element in the Earth's crust).[4-6] Nevertheless, reversible Ca metal anodes with compelling stripping/plating reaction kinetics remains inaccessible in most organic electrolytes.

The problem roots in two intrinsic constraints. First, compared to monovalent cations like Li^+ and Na^+, Ca^{2+} with stronger electrostatic interactions hinders the ion-pair dissociation, leading to sluggish ion transport in the bulk electrolyte and high energy barriers for ion desolvation at the anode/electrolyte interface.[7-9] Second, the aggressive decomposition of anions in organic electrolytes readily forms thick and ionic insulating inorganic phases on the surface of Ca metal, thus disabling the reversible Ca plating/stripping reactions (Figure 1a).[10-13] Given the critical role of electrolyte in determining the solid electrolyte interphase (SEI) chemistry and interfacial kinetics,[14-16] rational electrolyte design is under the spotlight for advancing Ca metal batteries. The first reversible Ca metal anode was achieved in a $Ca(BF_4)_2$-ethylene carbonate (EC)/propylene carbonate (PC) electrolyte.[17] The strong Ca^{2+}-BF_4^- ion pair coupling and the CaF_2-rich SEI layers demanded elevated temperatures of above 75 °C to activate effective Ca ion migration.[9] Room-temperature operation of Ca metal anodes was realized in a $Ca(BH_4)_2$/tetrahydrofuran (THF) electrolyte.[18] The relatively conductive CaH_2 component in the SEI from the BH_4^- decomposition was argued to enable Ca metal cycling at moderate overpotentials (< 0.5 V). However, the narrow electrochemical stability window (< 2.5V) and high cost of borohydride salts limit their practicality for Ca metal batteries using high-voltage cathodes. To weaken Ca^{2+}-anion coordination, large and weakly coordinating anions such as $[B(hfip)_4]^-$,[19, 20] $(CB_{11}H_{12})^-$,[21] and $[Al(hfip)_4]^-$[22] have been developed for reversible Ca metal anodes, but their practicality is limited by the expensive precursors and complex syntheses.

By contrast, $Ca(TFSI)_2$ is an affordable and widely available salt, but the strong Ca^{2+}-$TFSI^-$ couples in organic electrolytes have demonstrated irreversibility for Ca metal anodes. This behavior contrasts with the monovalent-ion (*i.e.,* Li^+, Na^+) electrolyte systems, which prefer weakly solvating solvents (e.g., fluorinated ethers) and enhanced contact-ion-pair (CIP) or aggregate (AGG) solvation structures to yield inorganic-rich SEI layers (*i.e.,* LiF, NaF), [23-25] thus stabilizing metal surfaces and promote uniform deposition of Li and Na metal anodes.[26, 27] In contrast, in the $Ca(TFSI)_2$-DME or EC/PC electrolytes, the tightly bound Ca^{2+}-$TFSI^-$ complexes indicate the formation of passivation layers mainly containing CaF_2, CaO and $CaCO_3$,[28, 29] which impose pronounced Ca^{2+} migration energy barriers (>1 eV).[1, 9, 30] To alleviate the formation of inorganic-rich SEI, strongly coordinating co-solvent (*i.e.*, 4-methoxybutan-2-amin added in $Ca[B(hfip)_4]_2$-DME (G1) electrolyte)[31] and ionic liquids (*i.e.,* $EmimBF_4$ added in $Ca(TFSI)_2$-dimethyl sulfoxide (DMSO) electrolyte)[32] have been introduced to decrease the coordination between anions and Ca^{2+}. Although the cycling lifespan of Ca metal anodes was extended, the overpotential remains above 0.5 V. Therefore, developing new electrolytes or strategies that can unlock $Ca(TFSI)_2$-based electrolytes enabling reversible Ca plating/stripping with low overpotentials remains challenging.

In this work, we introduce a two-pronged approach by systematically screening strongly coordinating solvent to reinforce Ca^{2+}-solvent coordination (Figure 1b) and an anion-pulling additive 1,2-dibromobenzene (1,2-DBB) to further extract $TFSI^-$ out of the primary solvation shell in $Ca(TFSI)_2$-based electrolytes (Figure 1c). Theoretical calculations of solvation strengths across a series of solvents (*i.e.*, ethers, carbonates, amides, and sulfoxides) in $Ca(TFSI)_2$-based electrolyte solutions, correlated with the electrochemical responses of Ca metal anodes in them, reveal a direct relationship between Ca reversibility and the ion-pair decoupling capability, thus identifying dimethylacetamide (DMAc) as the optimal solvent in this system. Although DMAc solvent has been explored for Ca anodes, strong cation-anion coupling persists and interfacial kinetics remain sluggish,[33] necessitating the introduction of "anion-pulling" chemistry to overcome this performance hurdle. By comparing the binding energies of halogen-benzene molecules with $TFSI^-$, 1,2-dibromobenzene (1,2-DBB) is selected as an effective additive for weakening Ca^{2+}-$TFSI^-$ coordination. Spectroscopic and theoretical analyses demonstrate that 1,2-DBB additive modulates the solvation structure and increases the chemical bond orders of TFSI$^-$ anions, thereby suppressing the decomposition of TFSI$^-$ into unfavorable inorganic compounds in the SEI as demonstrated by high-resolution transmission electron microscopy (HRTEM) observations. The resulting $Ca(TFSI)_2$-DMAc/1,2-DBB electrolyte exhibits high ionic conductivity (σ = 12.75 mS cm^{-2}), low desolvation energy barriers (ΔE = 27.02 kJ mol^{-1}), and accelerated Ca^{2+} transport kinetics through the electrode/electrolyte interface. Consequently, Ca//Ca symmetric cells operate with low overpotentials (< 0.2V vs. > 5V in conventional $Ca(TFSI)_2$-G1, EC/PC, or THF electrolytes) and extended cycle life (over 340 hours). The superiority of our anion-decoupled electrolytes is also demonstrated in the excellent cyclability of Ca//graphite (over 200 cycles with > 90% capacity retention) and Ca//9,10-phenanthrenequinone (PQ) full cells (290 cycles at 50 mA g^{-1}). Overall, this work unlocks the feasibility of $Ca(TFSI)_2$-based electrolytes that are previously unworkable for Ca metal anodes through the anion-decoupling chemistry. Our findings emphasize fundamentally different electrolyte design principles from these established in monovalent metal anode systems, offering new insights towards developing feasible electrolytes in multivalent metal batteries.

2. Results and discussion

2.1 Strongly coordinating solvents for decoupling Ca^{2+}-TFSI$^-$ pairs

Density functional theory (DFT) calculations of the binding energy differences (ΔE) between the representative alkali and alkaline earth metal ions (*e.g.,* Li^+, Na^+, K^+, Ca^{2+}, and Mg^{2+}) with typical solvents (*e.g.,* G1, THF, and EC) and with TFSI$^-$ anions, reveal that ΔE for divalent ions (Ca^{2+}, Mg^{2+}) are two times higher than those of monovalent ions (Li^+, Na^+, K^+) across all the representative solvents (Figure 2a). This result illustrates the stronger cation-anion coupling strength in Ca-based electrolyte systems. Notably, Ca^{2+} presents stronger binding energies with TFSI$^-$ than FSI$^-$, OTF$^-$, BF_4^- (Figure S1), highlighting the difficulty in decoupling Ca^{2+}-TFSI$^-$ ion pairs in the electrolyte. Furthermore, the lowest unoccupied molecular orbital (LUMO) energy levels of TFSI$^-$ shift markedly from 0.12 eV (free anion) to -0.68 eV upon coupling with Ca^{2+} (Figure S2a). The strong Ca^{2+}-TFSI$^-$ interaction reduces the Mayer bond orders across the internal bonds (C-F, S-N, S-O) in TFSI$^-$, thus enhancing their cleavage tendency to form CaF_2-rich SEI (Figure S2b).[34] It was reported that CaF_2 exhibits the largest Ca^{2+} migration energy barriers (~2046 meV) among the potential inorganic SEI components (*i.e.,* ~997 meV for CaO,

View Article Online
DOI: 10.1039/D5EE07317K

~540 meV for CaH_2, ~1436 meV for $CaCO_3$).[9] Therefore, it is essential to exclude $TFSI^-$ from the primary solvation shell and suppress its decomposition for feasible Ca metal cycling in the $Ca(TFSI)_2$-based electrolytes.

To approach a solvent-rich and anion-poor solvation configuration, we examined the donor number (DN) and the minimum electrostatic potential (ESP_{min}) of ten representative solvent molecules, including ethers, carbonates, amides, and sulfoxide. The DN reflects the tendency of electron donating ability of a solvent towards cations,[35] while ESP_{min} represents the lowest electrostatic potential on the solvent surface, indicating the strength of cation-solvent interactions.[36] Accordingly, solvents with high DN and large $|ESP_{min}|$ are expected to deliver strong coordination to Ca^{2+}. Figure S3 and Figure 2b summarizes the $|ESP_{min}|$ and DN distributions of nine representative solvents, which shows that dimethylformamide (DMF), DMAc and DMSO, belonging to amides, lie in the upper-right region with DN > 26 kcal mol^{-1}, $|ESP_{min}|$ > 44 kcal mol^{-1}, identifying them as highly coordinating solvent candidates. Ethers (*i.e.,* dioxolane DOL, G1, diglyme G2, tetraglyme G4) and carbonates (*i.e.,* EC, PC) present relatively low DN (<15 kcal mol^{-1}) or $|ESP_{min}|$ (< 30 kcal mol^{-1}).

To validate this prediction, Raman measurements and molecular dynamics (MD) simulations were performed for 0.3 M $Ca(TFSI)_2$ G1 (weakly coordinating solvent) and 0.3 M $Ca(TFSI)_2$ DMAc (strongly coordinating solvent) electrolyte solutions. Raman spectra related to the S-N-S vibration of $TFSI^-$ reveal that the coordinated $TFSI^-$ species (at 749.5cm^{-1}) predominate in the G1-based electrolyte, whereas the free $TFSI^-$ peak (at 738.9 cm^{-1}) is more pronounced in the DMAc-based electrolyte (Figure S4). MD simulations further reveal the distinct solvation features: the $Ca(TFSI)_2$-G1 electrolyte exhibits pronounced aggregations of Ca^{2+}-$TFSI^-$ ion pairs (Figure S5a) whereas $Ca(TFSI)_2$-DMAc displaces more dispersed solvated ion pair configurations (Figure S5b). Radial distribution functions (RDFs) show a higher coordination number of 3.5 for Ca-O_{TFSI^-} (oxygen in $TFSI^-$) in $Ca(TFSI)_2$-G1 electrolyte than the 2.1 in the $Ca(TFSI)_2$-DMAc electrolyte (Figure S5c), indicating more Ca^{2+}-$TFSI^-$ ion pairs in the former electrolyte. On the other hand, the coordination number for the solvent (Ca-$O_{Solvent}$) increases from 4.6 in the G1-based electrolyte to 5.7 in the DMAc-based electrolyte (Figure S5d). These comparisons corroborate the effectiveness of DMAc solvent with high DN and $|ESP_{min}|$ values in decoupling $TFSI^-$ from Ca^{2+}.

View Article Online
DOI: 10.1039/D5EE07317K

The improved ion decoupling translates directly to enhanced ion transport in the bulk electrolyte. Strongly coordinating electrolytes (0.3 M $Ca(TFSI)_2$ in DMF, DMAc, or DMSO) exhibit higher ionic conductivities (σ = 6.84 to 15.05 mS cm^{-2}) than the moderate or weakly solvating systems (σ = 0.58 to 3.67 mS cm^{-2}) under the identical 0.3 M salt concentration (Figure 2c and Figure S6). Interestingly, galvanostatic cycling of Ca//Ca symmetric cells in these electrolytes at 0.1 mA cm^{-2} and 0.1 mAh cm^{-2} (Figure 2e) display reversibility only in the DMF, DMAc, and DMSO-based electrolyte, whereas the cells employing the G1, G2, G4, THF, DOL and EC/PC-based electrolyte rapidly fail by exceeding the 5 V cutoff voltage.

Among the three workable electrolytes, the cyclability of Ca//Ca cells follows the order of DMAc (160 h) > DMF (100 h) > DMSO (40 h) at 0.1 mA cm^{-2}, despite the calculated binding energies between solvents and Ca^{2+} following a different trend (DMSO > DMAc > DMF, Figure S7). This discrepancy suggests that, beyond solvation strength, the electrochemical stability of Ca^{2+}-solvent-$TFSI^-$ complexes and the resulting SEI composition play unignorable role in determining reversibility of Ca metal anodes. Accordingly, we calculated the LUMO levels of Ca^{2+}-solvent-$TFSI^-$ (solvent = DMF, DMAc, DMSO) complexes and analyzed the LUMO contributions from $TFSI^-$ (Figure 2d). Although their overall LUMO levels are comparable (-0.59 to -0.72 eV), corresponding to similar reductive stability, the $TFSI^-$ contributions to LUMO are largely different, namely, 49.3% for Ca^{2+}-DMAc-$TFSI^-$, 61.3% for Ca^{2+}-DMF-$TFSI^-$, and 84.1% for Ca^{2+}-DMSO-$TFSI^-$. Interestingly, the observed cyclability (DMAc > DMF > DMSO) of Ca electrodes correlated inversely with the $TFSI^-$ contribution to LUMO. It means that higher $TFSI^-$ stability in the Ca^{2+}-solvent-$TFSI^-$ complex can suppress $TFSI^-$ decomposition into unfavorable inorganic SEI species, thus stabilizing the electrochemical reduction of Ca metal anodes. Overall, these results establish that strong Ca^{2+} solvating capability and the high stabilization degree of $TFSI^-$ can be considered as the primary criteria for selecting optimal solvents in $Ca(TFSI)_2$-based electrolytes. Having established DMAc as the ideal solvent, we further evaluated the concentration-dependent anion-coupling behavior. The physiochemical properties of electrolytes and resulting electrochemical performance of Ca electrodes recommend 0.3 M $Ca(TFSI)_2$-DMAc as the optimal choice (Figure S8).

View Article Online
DOI: 10.1039/D5EE07317K

2.2 Anion-pulling halogen benzene additives

Despite the reversibility achieved in Ca(TFSI)$_2$-DMAc electrolytes, the high overpotentials of >1 V for Ca metal plating/stripping reactions remain unsatisfactory. To further ameliorate the reaction kinetics, a series of halogenated benzenes was screened as anion-pulling additives to further decouple the Ca^{2+}-TFSI$^-$ ion pairs. The polarizable aromatic framework and electron-withdrawing halogens confer strong electropositivity for the aromatic C-H bonds (Figure S9), which favors the formation of C-H···O hydrogen bonds with TFSI$^-$. Figure S10a presents the C-H···O binding energies of various halogenated benzenes and DMAc with TFSI$^-$, namely, -36.86 kJ mol^{-1} for 1,2-dichlorobenzene (1,2-DCB), -37.28 kJ mol^{-1} for 1,2-DBB, -34.78 kJ mol^{-1} for 1,2-difluorobenzene (1,2-DFB), and -34.96 kJ mol^{-1} for DMAc, respectively. Remarkably, the Ca deposition/stripping overpotential decreases near linearly with increasing C-H···O binding energies, reaching a minimum of 0.32 V at 0.2 mA cm^{-2} in the 0.3 M Ca(TFSI)$_2$-DMAc/1,2-DBB electrolyte (Figure 3a and Figure S10b). The 1.1 V reduction from Ca(TFSI)$_2$-DMAc to Ca(TFSI)$_2$-DMAc/1,2-DBB suggests the effectiveness of the anion-pulling strategy. It is noted that although 1,2-DFB and DMAc present comparable binding energies with TFSI$^-$, the 1,2-DFB additive significantly increases the overpotential to 3.2 V (from 1.4 V for the baseline DMAc electrolyte), which is likely attributable to the 1,2-DFB-derived fluorinated inorganic species in the SEI layer.

For the interaction between 1,2-DBB additives and Ca^{2+}, DFT calculations exhibit markedly lower |ESP$_{\mathrm{min}}$| values (*i.e.*, 14.79 kcal mol^{-1} for 1,2-DBB *vs.* 45.78 kcal mol^{-1} for DMAc) and binding energies (*i.e.*, -83.83 kcal mol^{-1} for Ca^{2+}-1,2-DBB vs. -115.19 kcal mol^{-1} for Ca^{2+}-DMAc) (Figure S11). It is inferred that the 1,2-DBB additive does not enter the first solvation shell but instead exerts its pulling effect externally on TFSI$^-$. Other bromine benzene additives with different number of bromine substituents, like 1-Bromobenzene (1-BB) and 1,3,5-Tribromobenzene (1,3,5-TBB), were also examined that present lower binding energies with TFSI$^-$ and inferior electrochemical performance for Ca metal anodes (Figure S12). By cycling Ca//Ca symmetric cells in DMAc/1,2-DBB electrolytes with different 1,2-DBB ratios (0.1 vol%, 0.2 vol%, 0.5 vol%, and 1.0 vol%, Figure S13), the 0.5 vol% 1,2-DBB was determined as the optimal choice with the best cyclability of Ca metal for the subsequent studies.

Raman and nuclear magnetic resonance (NMR) measurements were carried out to evaluate

View Article Online
DOI: 10.1039/D5EE07317K

the solvation perturbation induced by 1,2-DBB. Upon dissolving Ca(TFSI)$_2$ in DMAc, the characteristic Raman peak at 1143.8 cm^{-1} referring to the S=O vibration of TFSI$^-$ downshifts to 1141.5 cm^{-1}, and further to 1140.4 cm^{-1} with 1,2-DBB addition (Figure 3c), signifying noticeable decoupling of TFSI$^-$ anions. The strong interaction between TFSI$^-$ and 1,2-DBB is further evidenced by the concurrent redshifts in the C-H in-plane and C-C-C out-of-plane bending vibrations of 1,2-DBB Raman spectra (Figure S14). These spectral changes can be attributed to the redistribution of electron density at the C-H donor site and distortion of the aromatic ring in 1,2-DBB upon binding with TFSI$^-$.[37] Moreover, the downfield shift of ^{1}H NMR peaks for 1,2-DBB (at both 0.5 vol% and 3 vol% concentrations) further illustrates the electron-withdrawing effect of the C-H sites in 1,2-DBB on TFSI$^-$ (Figure 3d). Similarly, the downfield shift in the ^{19}F NMR chemical shifts of TFSI$^-$ anions upon adding 1,2-DBB (Figure S15) also supports the anion-pulling mechanism.[38]

The binding configurations between TFSI$^-$ and DMAc or 1,2-DBB were calculated by DFT. It shows a shorter C-H···O length of 2.40 Å for 1,2-DBB-TFSI$^-$ than the 2.66 Å for DMAc-TFSI$^-$ (Figure S16a). Meanwhile, enhanced C-F, S-N and S-O bonding orders in TFSI$^-$ upon bonding with 1,2-DBB suggests greater thermodynamic stability of TFSI$^-$ (Figure S16b). The strong noncovalent interactions were further visualized via interaction region indicator (IRI) isosurfaces (Figure 3b).[39] MD simulations reveal that 1,2-DBB forms external complexes with TFSI$^-$ without entering the primary Ca^{2+} solvation shell (Figure 3e). RDFs (Figure 3f and 3g) show that the coordination numbers of Ca-O$_{TFSI^-}$ decrease from 2.1 to 1.5, while the Ca-O$_{DMAc}$ increases from 5.7 to 6.3 to preserve solvation stability. Critically, 1,2-DBB was not observed in the primary solvation shell, consistent with their weaker binding energy to Ca^{2+} (Figure S17). The rearrangement of DMAc coordination was further validated by spectroscopic evidence: the downshifts of ^{13}C NMR chemical shift (Figure 3h and Figure S18) in DMAc solvent following the 1,2-DBB addition indicated enhanced Ca^{2+}-DMAc interaction. This enhancement is corroborated by Raman spectra, which reveal an increased percentage of coordinated DMAc molecules from 42.7% to 49.2% (Figure S19). The effective anion-decoupling resulted in an increased ionic conductivity from 11.57 to 12.75 mS cm^{-2} (Figure S20), confirming the accelerated Ca^{2+} transport in the DMAc/1,2-DBB electrolyte.

Building on the MD-derived coordination number (7.8), a representative Ca^{2+} solvation structure comprising five DMAc and one $TFSI^-$ anion was modeled. In the presence of 1,2-DBB, DFT results show elongated and weakened Ca^{2+}-$TFSI^-$ bonds arising from the extraction of $TFSI^-$ from solvation shell by 1,2-DBB. Conversely, the Ca^{2+}-DMAc coordination presents shorter bond lengths and higher bond orders to compensate for the Ca^{2+} polarization left by $TFSI^-$ deficiency (Figure S21). Moreover, the presence of 1,2-DBB reduces the desolvation free energy of Ca^{2+}, reaching a minimum upon complete $TFSI^-$ removal, indicating that anion decoupling accelerates desolvation kinetics (Figure 2i). Temperature-dependent electrochemical impedance spectroscopy (EIS) analyses (Figure 2j and Figure S22) also reveal lower Ca^{2+} desolvation energies in DMAc/1,2-DBB electrolyte ($\Delta E = 27.02$ kJ mol^{-1}) compared with pristine DMAc ($\Delta E = 51.55$ kJ mol^{-1}), consistent with the faster interfacial kinetics. In addition, the $TFSI^-$ contribution to the LUMO decreases from 11.1% to 3.4% upon 1,2-DBB addition (Figure S23), suggesting improved reductive stability of $TFSI^-$ and regulated SEI chemistry to be discussed below.

2.3 Solid electrolyte interphases from anion-decoupled electrolytes

The anion-decoupling strategy not only facilitates ion transport in bulk electrolyte and the Ca^{2+} desolvation kinetics at the electrolyte/electrode interface but also importantly influences the SEI composition and Ca stripping/plating behaviors. After 20 cycles in Ca//Ca symmetric cells in the DMAc electrolyte, the cycled Ca anodes were covered by a fluorine (F)-rich passivation layer (Figure 4a) in comparison to pristine Ca foil (Figure S24a-b). XRD analysis identifies crystalline $Ca(OH)_2$, CaO, CaF_2 as the dominant inorganic species on Ca metal surface (Figure 4c). In contrast, Ca metal electrodes cycled in the DMAc/1,2-DBB electrolyte present a uniform surface with significantly reduced F content (Figure 4b and Figure S24c), consistent with the negligible CaF_2 peaks in the XRD result. HRTEM was employed to examine the microstructure and composition of SEI. Ca metal anodes cycled in the DMAc electrolyte present a thick SEI layer (~23.5 nm) containing CaF_2 nanocrystals with lattice fringe of 0.273 nm (Figure 4d). The SEI formed in the DMAc/1,2-DBB electrolyte is thinner (~11.5 nm) and shows amorphous organic on the surface of metallic Ca deposits (Figure 4e). Furthermore, characterizations of SEI layers formed in the DMAc/1,2-DCB and DMAc/1,2-DFB electrolytes reveal a clear correlation between the anion-decoupling ability of the additives and the resulting SEI properties (Figure S25).

View Article Online
DOI: 10.1039/D5EE07317K

The chemical composition and depth distribution of SEI layers was further elucidated by X-ray photoelectron spectroscopy (XPS) depth profiling and time-of-flight secondary ion mass spectrometry (TOF-SIMS). After cycling in the DMAc electrolyte, the F 1s spectrum shows a high content of Ca-F species (Figure S26a), which become more prominent with increasing Ar^+ etching time. This result indicates abundant CaF_2 throughout the SEI layer on Ca metal surface, a consequence of aggressive $TFSI^-$ decomposition. Conversely, in the DMAc/1,2-DBB electrolyte, the normalized F 1s peak intensities for inorganic species are much lower (Figure S26b) along with increased $C\text{-}F_x$ peaks (Figure S27). Such a difference confirms the suppressed $TFSI^-$ decomposition and stabilization of C-F bonds by the 1,2-DBB additive. Similar trends are also observed in the S 2p and N 1s spectrum (Figure S28 and S29).

XPS depth profiling revealed a hierarchical SEI structure in the DMAc electrolyte, where the inorganic components (*i.e.,* CaF_2, CaS_x) from $TFSI^-$ decomposition become increasingly prominent upon etching, while organic components diminished rapidly with depth (Figure S27). Conversely, the SEI from the DMAc/1,2-DBB electrolyte exhibited reduced inorganic content and abundant organic components upon etching, indicating the formation of a solvent-derived, organic-rich SEI promoted by anion-pulling effect. These SEI characteristics were further corroborated by TOF-SIMS. The SEI formed in the DMAc/1,2-DBB electrolyte was dominated by solvent-derived organic species (CN^-, C_2^-), alongside minor inorganic fluorides (Figures 4f-h and Figure S30). In contrast, SEI derived from the DMAc electrolyte shows a high prevalence of CaF^+, Ca_2OF^+, $Ca_3O_2F^+$ throughout the depth, while organic components are rich only on the top surface (Figure 4g and Figure S31a-c). Sulfur-containing species (S^-, SO^-, SO_2^-), which are solely derived from $TFSI^-$ anions, are also greatly reduced upon 1,2-DBB addition (Figure S31d). Quantitative analysis of the organic-to-inorganic component (O/I) ratios from TOF-SIMS depth profiles (Figure 4h) highlights this contrast: the internal SEI formed in the DMAc/1,2-DBB electrolyte reached an O/I value of 2.1, compared to 0.8 for the SEI in DMAc electrolyte demonstrates the suppression of $TFSI^-$ decomposition. To confirm superiority of the organic-rich SEI, an electrolyte replacement protocol was implemented (Figure 4i-j). When cycled directly in the DMAc electrolyte, $TFSI^-$-derived SEI with sluggish Ca^{2+} diffusion feature results in a high overpotential of 1.27 V. In contrast, Ca metal electrodes pre-cycled in the DMAc/1,2-DBB electrolyte and subsequently transferred to the DMAc electrolyte exhibited a

View Article Online
DOI: 10.1039/D5EE07317K

much lower overpotential of 0.55 V, indicating the persistent benefit of the pre-formed organic-rich SEI.

To evaluate the possible reduction of 1,2-DBB additive on Ca metal, Ca electrodes were immersed in pure 1,2-DBB for 24 h before assembling symmetric cells with DMAc electrolyte. The resulting voltage profiles remain unchanged relative to the untreated Ca//Ca cells (Figure S32). Furthermore, in-situ Raman spectroscopy monitored the electrolyte evolution during cycling (Figure S33). The 1,2-DBB signal at 399.1 cm^{-1} remained constant in both intensity and peak position, whereas the characteristic DMAc peak at 589.7 cm^{-1} presents apparent attenuation during the initial cycles before approaching stabilization. Consistently, no bromine-containing species were detected in TOF-SIMS spectrum for the SEI (Figure S34). These results collectively demonstrate that 1,2-DBB acts solely as an anion-pulling modulator without direct participation in interfacial reactions, which differs from the reported role of 1,2-DBB decomposition in forming a NaBr-rich SEI in Na metal batteries.[40]

2.4 Electrochemical performance of Ca metal anodes

To validate the efficacy of the anion-decoupled electrolyte, electrochemical performance of Ca metal anodes was systematically evaluated. As shown in Figure 5a, the Ca//Ca symmetric cell in the DMAc/1,2-DBB electrolyte achieves an extended cycling lifetime of 340 h at 0.05 mA cm^{-2} and 0.025 mAh cm^{-2}. In comparison with the high overpotential of 1.68 V in the DMAc electrolyte, the overpotential reduced by nearly ninefold to 0.19 V. Event under a tenfold higher current density of 0.5 mA cm^{-2}, the cells with DMAc/1,2-DBB electrolyte persisted stability over 65 cycles (Figure S35). Furthermore, the DMAc/1,2-DBB electrolyte enabled superior rate capability (Figure 5b), reducing the overpotentials by two to five times compared to DMAc electrolyte across current densities ranging from 0.1 to 2 mA cm^{-2} (Figure 5c). Consistently, the cyclic voltammetry (CV) profiles exhibited pronounced stripping and plating peak currents (Figure S36), indicative of enhanced reaction kinetics. Benchmarking against state-of-the-art Ca anode performance in various electrolytes highlights that the present anion-decoupled formulation achieves one of the best combinations of low overpotentials, high current responses, and extended cycling stability (Figure 5d and Table S1).[33, 41-44]

Electrochemical impedance spectroscopy (EIS) was employed to probe the interfacial kinetics and their evolution during cycling (Figure S37). For fresh cells, the charge transfer

View Article Online
DOI: 10.1039/D5EE07317K

resistance (R_{CT}) of Ca//Ca symmetric cells in the DMAc/1,2-DBB electrolyte are more than twenty times lower than that in the DMAc electrolyte (Figure S37a-b). Although impedances increased upon cycling for both systems, the cell with the DMAc/1,2-DBB electrolyte maintained exceptional interfacial stability, with both R_{CT} and SEI resistance (R_{SEI}) reduced by over seven times compared to those in the DMAc electrolyte after 20 cycles (Figure S37c-d), consistent with the low overpotential and superior rate performance.

CV curves of Ca//carbon paper (CC) asymmetric cells (Figure S38) exhibited reduced voltage hysteresis and larger current response in the DMAc/1,2-DBB electrolyte than these in the DMAc electrolyte. SEM images and corresponding EDS mapping demonstrated uniform Ca deposits on the CC current collector (Figure S39). To further verify the kinetic advantage in the DMAc/1,2-DBB electrolyte, we then paired Ca metal with graphite (Gra) electrodes undergoing rapid co-intercalation reaction in the DMAc-based electrolyte.[45, 46] In the DMAc system, Ca//Gra cells suffered severe polarization and negligible capacities due to the high overpotential and poor reversibility of Ca metal anodes (Figure S40). In contrast, the DMAc/1,2-DBB electrolyte enabled highly reversible discharge/charge over 200 cycles at 100 mA g^{-1} with a stable capacity of 78 mAh g^{-1} (Figure 5e). When the current density increased by 20-fold from 50 mA g^{-1} to 1000 mA g^{-1}, 79 % of the initial capacity was preserved (Figure 5f) with a distinct discharge plateau at 0.37 V throughout the high-rate cycling (Figure 5g). The remarkable high-rate capability can be attributed to the appealing reaction kinetics of Ca metal electrode. The Ca//9,10-phenanthrenequinone (PQ) full cell was also built to deliver decent cyclic capacities exceeding 90 mAh g^{-1} and stable cycling for over 290 cycles (Figure 5h and Figure S41), supporting the practical applicability of the tailored electrolyte in Ca-based energy storage, whereas it fails to deliver appreciable capacity in the DMAc electrolyte due to the severe kinetic limitation of the Ca anode (Figure S42). When extended to other fluorinated Ca salts (*i.e.,* $Ca(BF_4)_2$ and $Ca(OTf)_2$), the addition of 1,2-DBB can also significantly reduce the Ca plating/stripping overpotentials, which suggests the broad applicability of our anion-decoupling strategy across diverse Ca electrolytes (Figure S43). Finally, we also prove the effectiveness of our anion-decoupling strategy for Mg metal anodes by cycling Mg//Mg cells in $Mg(TFSI)_2$-G1, DMAc, and DMAc/1,2-DBB electrolytes, where similar reductions in the plating/stripping overpotentials are observed (Figure S44), implying the general applicability

View Article Online
DOI: 10.1039/D5EE07317K

of this electrolyte design principle for multivalent metal anodes.

3. Conclusion

In summary, we revealed the critical role of anion-decoupling chemistry in enhancing the reaction kinetics and cycling stability of Ca metal anodes in Ca(TFSI)$_2$-based electrolytes. By integrating strongly coordinating DMAc solvent with the anion-pulling 1,2-DBB additive, the Ca^{2+}-TFSI$^-$ coupling is significantly weakened, rendering the strength Ca^{2+}-solvent coordination, high ionic conductivity (12.75 mS cm^{-2}), and reduced desolvation energy barriers at the electrode/electrolyte interface. More importantly, this decoupling strategy improves the stability of TFSI$^-$ and suppresses its decomposition into undesirable inorganic compounds. The organic-rich SEI from solvent-rich electrolyte configuration facilitates Ca^{2+} transport and electrodeposition with low overpotentials. Effectiveness of the anion-decoupled electrolyte is demonstrated by the stable cycling of Ca//Ca symmetric cells in the Ca(TFSI)$_2$-DMAc/1,2-DBB electrolyte, in comparison to the high overpotentials of >5 V and short cycle life of Ca metal electrodes in conventional electrolytes. The anion-decoupled DMAc/1,2-DBB electrolyte also sustain Ca//Gra and Ca//PQ full cells over 200 cycles with >90% capacity retention. These findings highlight a unique electrolyte design paradigm, fundamentally distinct from monovalent metal anodes which prefer strong anion coordination in the electrolyte systems, offering new insights for advancing sustainable and safe multivalent metal anodes.

Author Contributions

Conceptualization, methodology and formal analysis: Q. Meng, Z.-L. Xu; data curation, investigation, project administration, visualization and writing-original draft: Q. Meng; resources and validation: Z. Zhan; funding acquisition and resources: Z.-L. Xu, Y. Y. Ma, Q. Qi, Y. K. Hua, Y. Y. Yi, J. Y. Yu, M. C. Wu; supervision: Z.-L. Xu; writing-reviewing and editing: J. J. Tang, S. H. Cai, K. C. Chan and Z.-L. Xu.

Acknowledgements

This work described in this paper was fully supported by grants from the Research Grants Council of the Hong Kong Special Administrative Region, China (Project No. PolyU15305022, PolyU15304723), the Research Institute for Advanced Manufacturing (Project No. 1-CDLR),

View Article Online
DOI: 10.1039/D5EE07317K

the Research Committee of the Hong Kong Polytechnic University (Project No. G-UARH, 1-BBR0, 4-W43C), and the General Program Sponsored by Basic Research Fund in Shenzhen Natural Science Foundation (Project No. JCYJ20250604184257074).

References

1 J. Kim, M. Kim, J. Lee, J. An, S. Yang, H. C. Ahn, D.-J. Yoo and J. W. Choi, *Chem. Soc. Rev.*, 2024, **53**, 8878-8902.

2 Y. Liang, H. Dong, D. Aurbach and Y. Yao, *Nat. Energy*, 2020, **5**, 646-656.

3 H. Lin, J. Yu, F. Chen, R. Li, B. Y. Xia and Z. L. Xu, *Small Methods*, 2023, **7**, 2300561.

4 I. D. Hosein, *ACS Energy Lett.*, 2021, **6**, 1560-1565.

5 Y. Hua, Y. Ma, Q. Qi and Z.-L. Xu, *Nanoscale*, 2024, **16**, 17683-17698.

6 R. Li, Y. Lee, Z. Song, S. Ma, Y. Yi, H. Lin, Y. Hua, P. Jiang, F. Chen, J. Yu, X. Pu, Z. Chen, K. C. Chan, K.-Y. Park and Z.-L. Xu, *Adv. Mater.*, 2025, **37**, e06603.

7 S. Li, J. Zhang, S. Zhang, Q. Liu, H. Cheng, L. Fan, W. Zhang, X. Wang, Q. Wu and Y. Lu, *Nat. Energy*, 2024, **9**, 285-297.

8 M. E. Arroyo-de Dompablo, A. Ponrouch, P. Johansson and M. R. Palacín, *Chem. Rev.*, 2019, **120**, 6331-6357.

9 J. Forero-Saboya, C. Davoisne, R. Dedryvère, I. Yousef, P. Canepa and A. Ponrouch, *Energy Environ. Sci.*, 2020, **13**, 3423-3431.

10 D. Aurbach, R. Skaletsky and Y. Gofer, *J. Electrochem. Soc.*, 1991, **138**, 3536.

11 S. Yang, X. Wang, R. Li, Y. Zhou, H. Huang, M. Zhou, Y. Gao, W. Zhao, Y. Gao and Z. Pan, *Energy Environ. Sci.*, 2025, **18**, 1941-1951.

12 A. M. Melemed and B. M. Gallant, *J. Electrochem. Soc.*, 2020, **167**, 140543.

13 B. Ji, H. He, W. Yao and Y. Tang, *Adv. Mater.*, 2021, **33**, 2005501.

14 H. Wan, J. Xu and C. Wang, *Nat. Rev. Chem.*, 2024, **8**, 30-44.

15 X. Liu, X. Dong, H. Adenusi, Y. Wu and S. Passerini, *Nat. Rev. Chem.*, 2025, 1-12.

16 H. Lin, Z. Zhan, H. Zeng, R. Li, Y. Yi, F. Chen, S. Cai, Y. Zhu, C. F. Cheung and Z.-L. Xu, *Adv. Mater.*, 2025, **n/a**, e10711.

17 A. Ponrouch, C. Frontera, F. Barde and M. R. Palacin, *Nat. Mater.*, 2016, **15**, 169-172.

18 D. Wang, X. Gao, Y. Chen, L. Jin, C. Kuss and P. G. Bruce, *Nat. Mater.*, 2018, **17**, 16-

View Article Online
DOI: 10.1039/D5EE07317K

20.

19 Z. Li, O. Fuhr, M. Fichtner and Z. Zhao-Karger, *Energy Environ. Sci.*, 2019, **12**, 3496-3501.

20 A. Shyamsunder, L. E. Blanc, A. Assoud and L. F. Nazar, *ACS Energy Lett.*, 2019, **4**, 2271-2276.

21 K. Kisu, S. Kim, T. Shinohara, K. Zhao, A. Zuttel and S. I. Orimo, *Sci. Rep.*, 2021, **11**, 7563.

22 T. Pavcnik, J. D. Forero-Saboya, A. Ponrouch, A. Robba, R. Dominko and J. Bitenc, *J. Mater. Chem. A*, 2023, **11**, 14738-14747.

23 Y. Zhao, T. Zhou, M. Mensi, J. W. Choi and A. Coskun, *Nat. Commun.*, 2023, **14**, 299.

24 S. Wang, X.-G. Zhang, Y. Gu, S. Tang and Y. Fu, *J. Am. Chem. Soc.*, 2024, **146**, 3854-3860.

25 S. Ilic, S. N. Lavan and J. G. Connell, *Chem*, 2024, **10**, 2987-3007.

26 J. Tan, J. Matz, P. Dong, J. Shen and M. Ye, *Adv. Energy Mater.*, 2021, **11**, 2100046.

27 H. Yildirim, A. Kinaci, M. K. Y. Chan and J. P. Greeley, *ACS Appl. Mater. Interfaces*, 2015, **7**, 18985-18996.

28 J. D. Forero-Saboya, E. Marchante, R. B. Araujo, D. Monti, P. Johansson and A. Ponrouch, *J. Phys. Chem. C*, 2019, **123**, 29524-29532.

29 R. B. Araujo, V. Thangavel and P. Johansson, *Energy Storage Mater.*, 2021, **39**, 89-95.

30 Z. Hou, R. Zhou, Z. Min, Z. Lu and B. Zhang, *ACS Energy Lett.*, 2023, **8**, 274-279.

31 S. Hou, X. Ji, K. Gaskell, P.-f. Wang, L. Wang, J. Xu, R. Sun, O. Borodin and C. Wang, *Science*, 2021, **374**, 172-178.

32 L. Ye, M. Liao, K. Zhang, M. Zheng, Y. Jiang, X. Cheng, C. Wang, Q. Xu, C. Tang, P. Li, Y. Wen, Y. Xu, X. Sun, P. Chen, H. Sun, Y. Gao, Y. Zhang, B. Wang, J. Lu, H. Zhou, Y. Wang, Y. Xia, X. Xu and H. Peng, *Nature*, 2024, **626**, 313-318.

33 Z. Hou, R. Zhou, Y. Yao, Z. Min, Z. Lu, Y. Zhu, J. M. Tarascon and B. Zhang, *Angew. Chem., Int. Ed.*, 2022, **61**, e202214796.

34 I. Mayer, *J. Comput. Chem.*, 2007, **28**, 204-221.

35 P. Zhou, Y. Xiang and K. Liu, *Energy Environ. Sci.*, 2024, **17**, 8057-8077.

36 Y. Wu, Q. Hu, H. Liang, A. Wang, H. Xu, L. Wang and X. He, *Adv. Energy Mater.*,

View Article Online
DOI: 10.1039/D5EE07317K

2023, **13**, 2300259.

37 G. Shakila, S. Periandy and S. Ramalingam, *Spectrochim. Acta, Part A*, 2012, **86**, 449-455.

38 Z. Zhao, B. Nian, Y. Lei, L. Zhao, M. N. Hedhili, D. Guo, Z. Shi, W. Zhao, J. K. El-Demellawi and Y. Wang, *Adv. Mater.*, 2024, **36**, 2402626.

39 T. Lu and Q. Chen, *Chemistry-Methods*, 2021, **1**, 231-239.

40 L. Wang, N. Ren, Y. Yao, H. Yang, W. Jiang, Z. He, Y. Jiang, S. Jiao, L. Song, X. Wu, Z.-S. Wu and Y. Yu, *Angew. Chem., Int. Ed.*, 2023, **135**, e202214372.

41 Z. Hou, R. Zhou, K. Liu, J. Zhu and B. Zhang, *Angew. Chem., Int. Ed.*, 2025, **64**, e202413416.

42 H. Lin, J. Meng, W. Guo, R. Li, Y. Yi, Y. Ma, C. F. Cheung, D. Aurbach and Z.-L. Xu, *Energy Environ. Sci.*, 2024, **17**, 6548-6558.

43 S. Yang, X. Wang, R. Li, Y. Zhou, H. Huang, M. Zhou, Y. Gao, W. Zhao, Y. Gao, Z. Pan and X. Yang, *Energy Environ. Sci.*, 2025, **18**, 1941-1951.

44 Z. Slim, C. Cruz-Cardona, C. Pechberty, T. Hosaka, Z. Mandić, V. Panic and P. Johansson, *ACS Mater. Lett.*, 2025, **7**, 3235-3242.

45 Y. Yi, Y. Xing, H. Wang, Z. Zeng, Z. Sun, R. Li, H. Lin, Y. Ma, X. Pu, M. M. Li, K. Y. Park and Z. L. Xu, *Angew. Chem., Int. Ed.*, 2024, **63**, e202317177.

46 J. Park, Z.-L. Xu, G. Yoon, S. K. Park, J. Wang, H. Hyun, H. Park, J. Lim, Y.-J. Ko, Y. S. Yun and K. Kang, *Adv. Mater.*, 2020, **32**, 1904411.

View Article Online
DOI: 10.1039/D5EE07317K

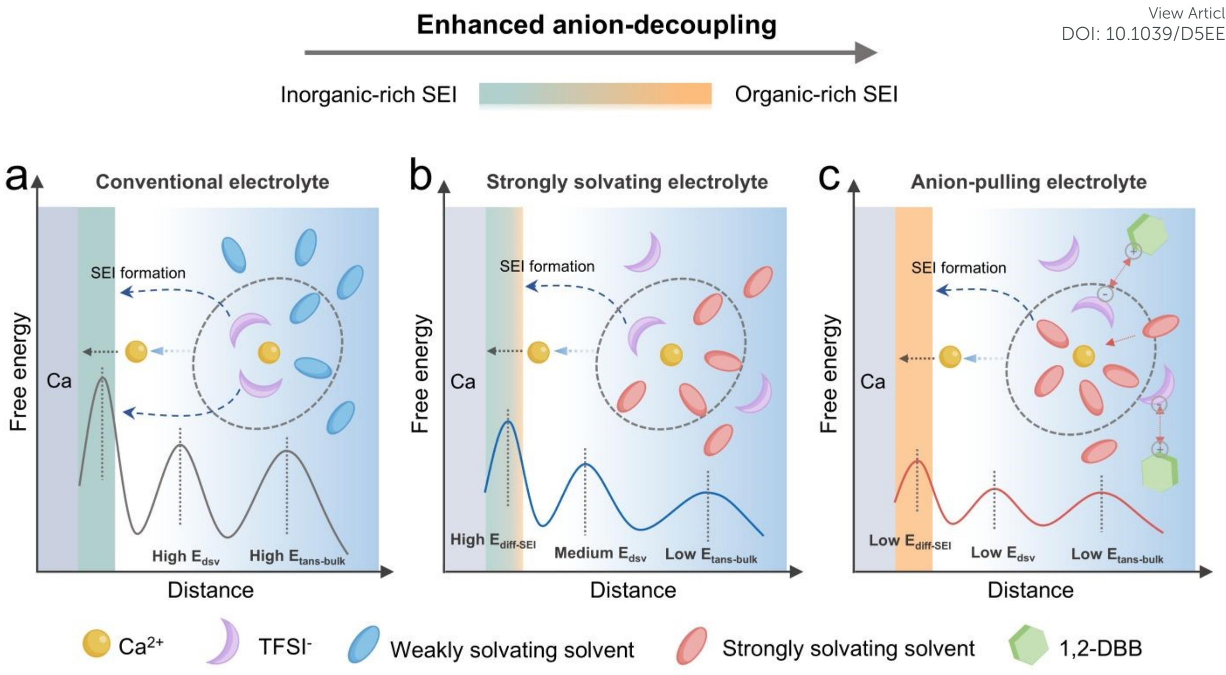

Figure 1. Schematic illustration of the anion-decoupling mechanism. The Ca^{2+} migration and reduction processes in (a) conventional electrolyte, (b) strongly solvating electrolyte and (c) anion-pulling electrolyte. $E_{trans\text{-}bulk}$, E_{dsv} and $E_{diff\text{-}SEI}$ represent the energy barriers for Ca^{2+} transport in the bulk electrolyte, desolvation at the interface, and diffusion through the SEI, respectively.

View Article Online
DOI: 10.1039/D5EE07317K

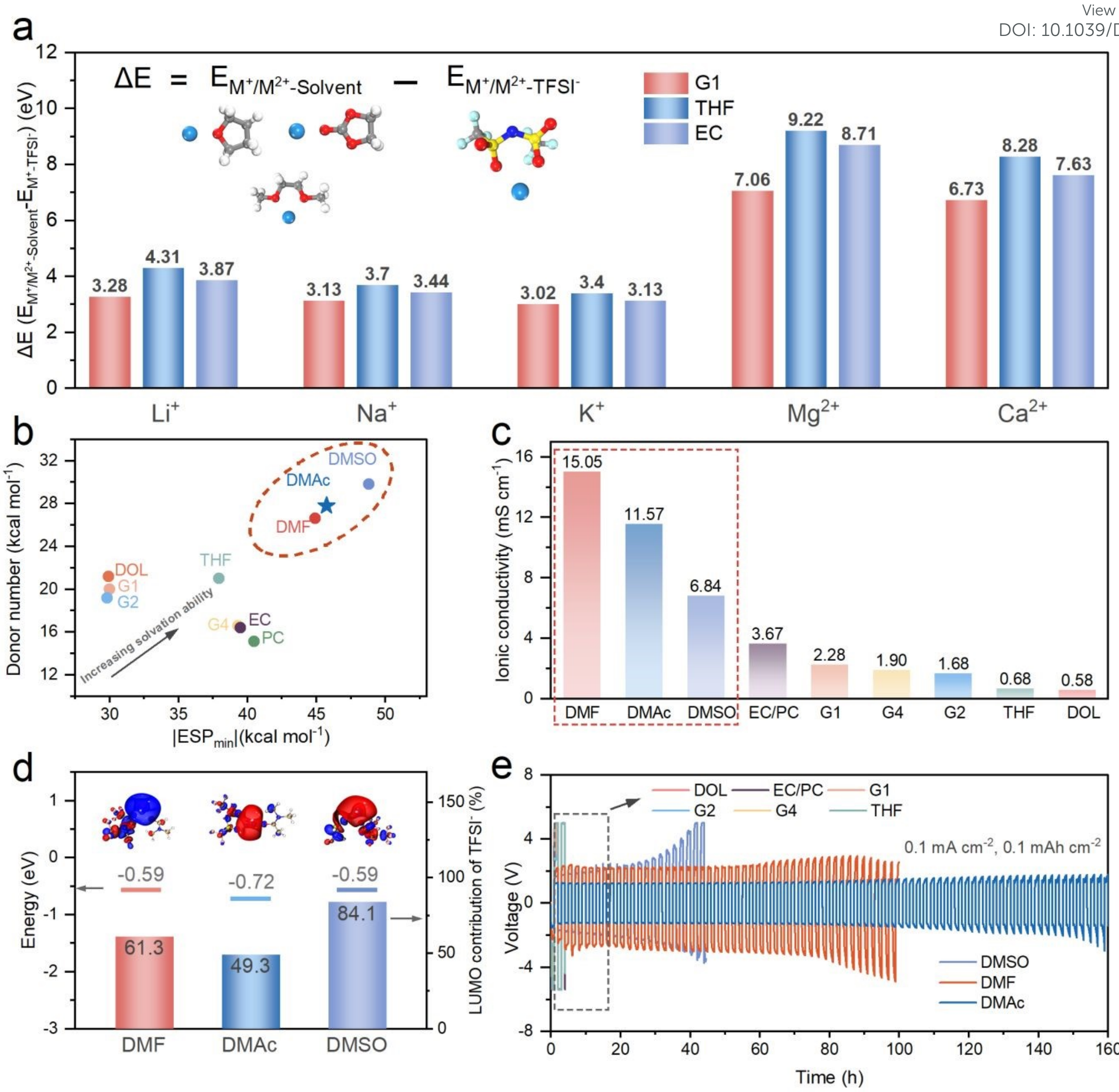

Figure 2. (a) Binding energy differences between cation-solvent and cation-anion ($\Delta E = E_{M\text{-}Solvent} - E_{M\text{-}TFSI^-}$) in M-TFSI/solvent electrolytes, M = Li^+, Na^+, K^+, Mg^{2+}, Ca^{2+}, solvent = G1, THF, EC. (b) DN vs. $|ESP_{min}|$ plots of nine representative solvents. (c) Ionic conductivities of 0.3 M $Ca(TFSI)_2$ in the solvents in (b). (d) LUMO energies and $TFSI^-$ LUMO contribution ratios of three Ca^{2+}-solvent-$TFSI^-$ (solvent = DMF, DMAc, DMSO) complexes. (e) Cycling performance of Ca//Ca symmetric cells in 0.3 M $Ca(TFSI)_2$ DMAc, DMF, and DMSO electrolytes at 0.1 mA cm^{-2} and 0.1 mAh cm^{-2}.

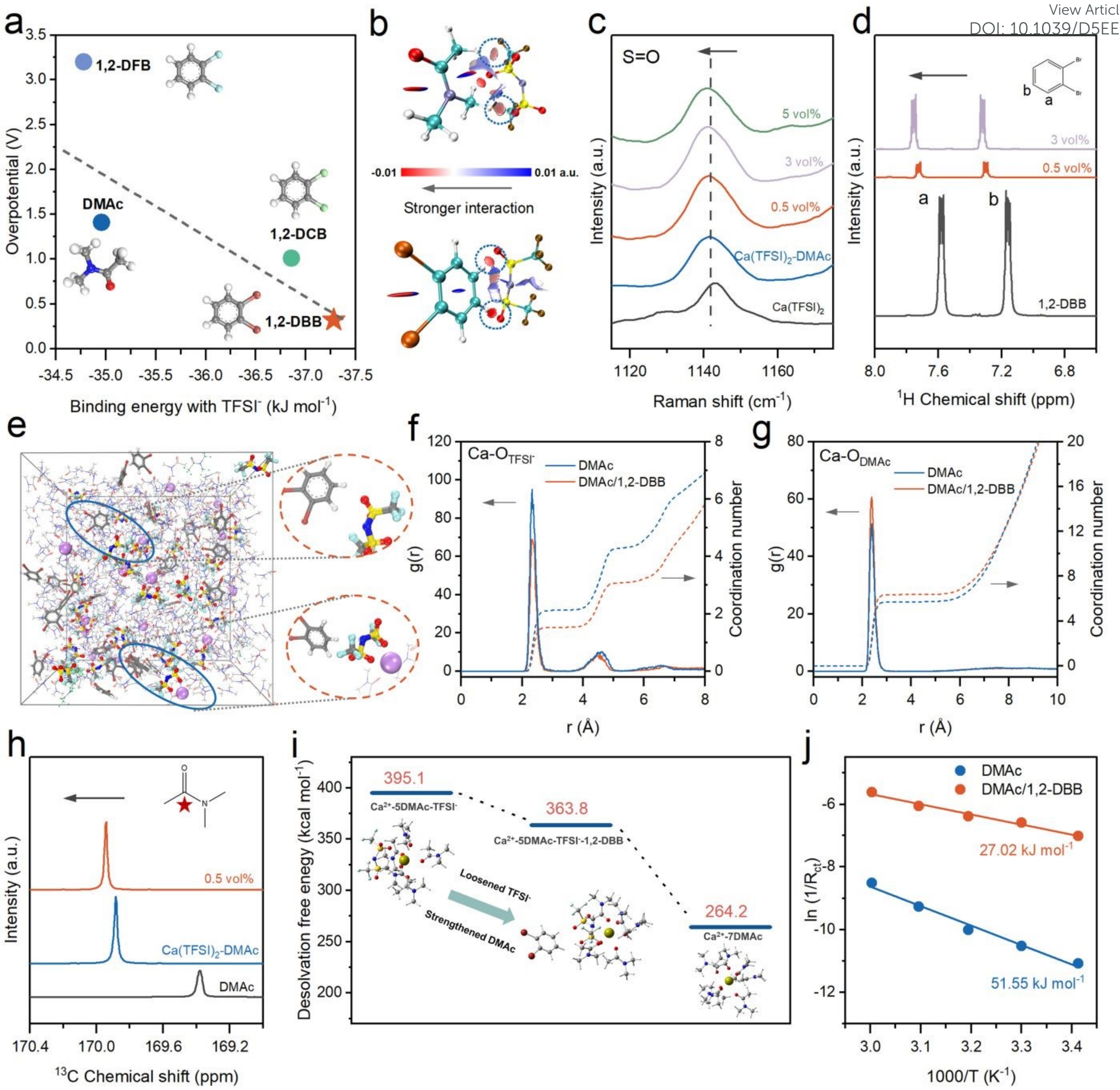

Figure 3. (a) Correlation between the binding energies of DMAc, 1,2-DFB, 1,2-DCB and 1,2-DBB with TFSI⁻ and the overpotentials of Ca//Ca symmetric cells cycling in corresponding electrolytes. (b) IRI isosurfaces image of noncovalent interactions between TFSI⁻ and DMAc (bottom) or 1,2-DBB (top). (c) Raman spectra of $Ca(TFSI)_2$ salt, DMAc electrolyte, DMAc/1,2-DBB electrolytes. (d) ^{1}H NMR spectra of pure 1,2-DBB and DMAc/1,2-DBB electrolytes with 0.5 vol% and 3 vol% 1,2-DBB. (e) The snapshot from the MD simulation box of the DMAc/1,2-DBB electrolyte. RDFs (solid lines) and coordination number (dashed lines) for (f) $Ca\text{-}O_{TFSI}^-$ and (g) $Ca\text{-}O_{DMAc}$ in different electrolytes. (h) ^{13}C NMR spectra of DMAc solvent, DMAc electrolyte, and DMAc/1,2-DBB electrolyte. (i) DFT calculated Ca^{2+} desolvation energies of different solvation structures. (j) Arrhenius plots to calculate the Ca^{2+} desolvation energies in the DMAc and DMAc/1,2-DBB electrolytes.

View Article Online
DOI: 10.1039/D5EE07317K

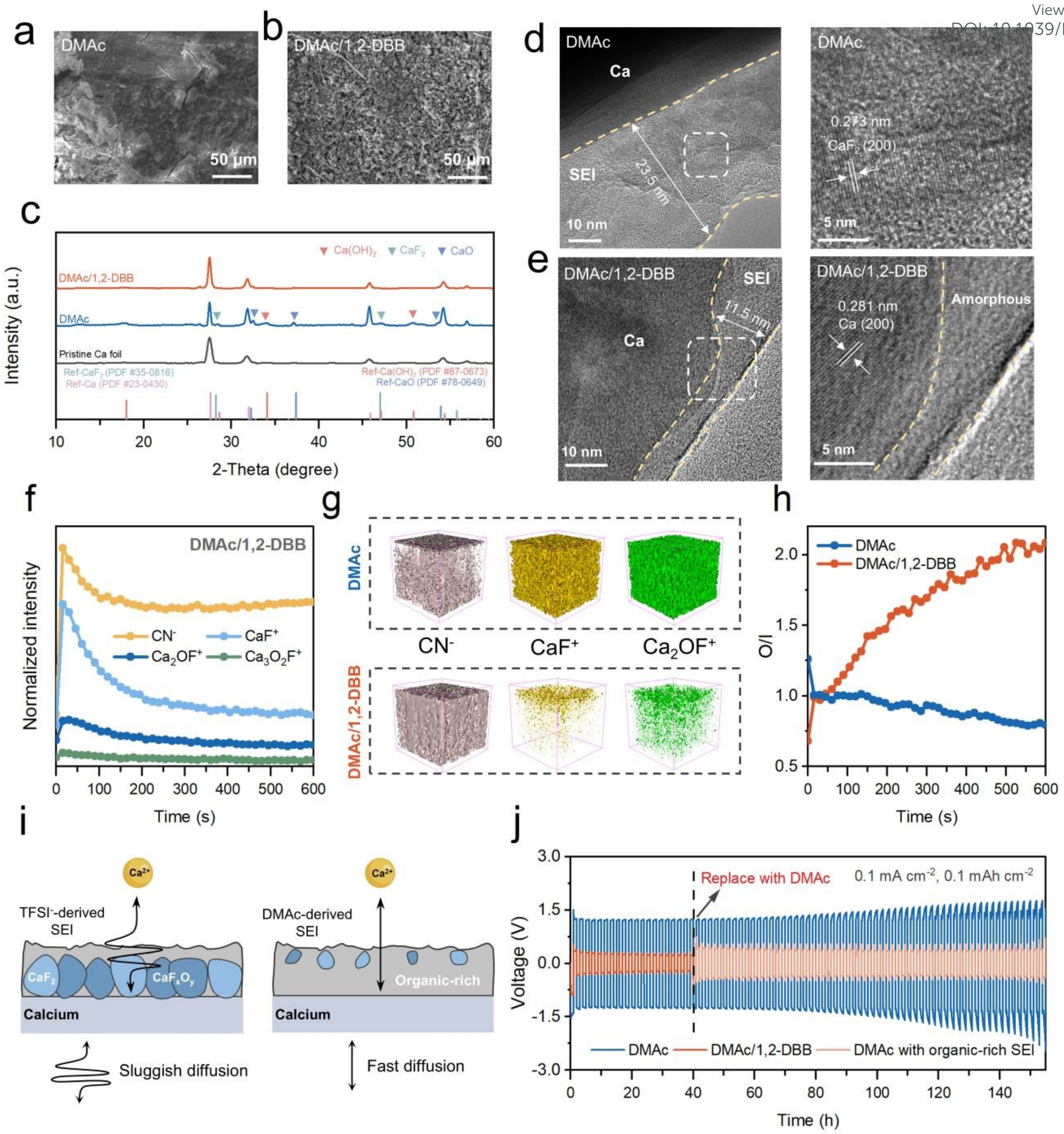

Figure 4. SEM images of cycled Ca metal anodes in the (a) DMAc and (b) DMAc/1,2-DBB electrolytes. (c) XRD patterns for the pristine Ca foil, Ca metal anodes cycled in DMAc, DMAc/1,2-DBB electrolytes. HRTEM images of SEI layers formed in the (d) DMAc and (e) DMAc/1,2-DBB electrolytes. (f) TOF-SIMS depth profiles of Ca anodes after cycling in the DMAc/1,2-DBB electrolyte. (g) TOF-SIMS 3D reconstruction of CN$^-$, CaF$^+$ and Ca$_2$OF$^+$ in SEI formed in DMAc electrolyte (up) and DMAc/1,2-DBB electrolyte (bottom). (h) The depth profile of the organic to inorganic components ratios (O/I) in SEI formed in these two electrolytes. (i) Schematic illustration of Ca^{2+} transport across inorganic-rich SEI (left) and organic-rich SEI (right) formed in DMAc and DMAc/1,2-DBB electrolytes, respectively. (j) Voltage profiles of Ca//Ca symmetric cells cycling in DMAc, DMAc/1,2-DBB (before 40th hour) + DMAc (after 40th hour) electrolytes.

View Article Online
DOI: 10.1039/D5EE07317K

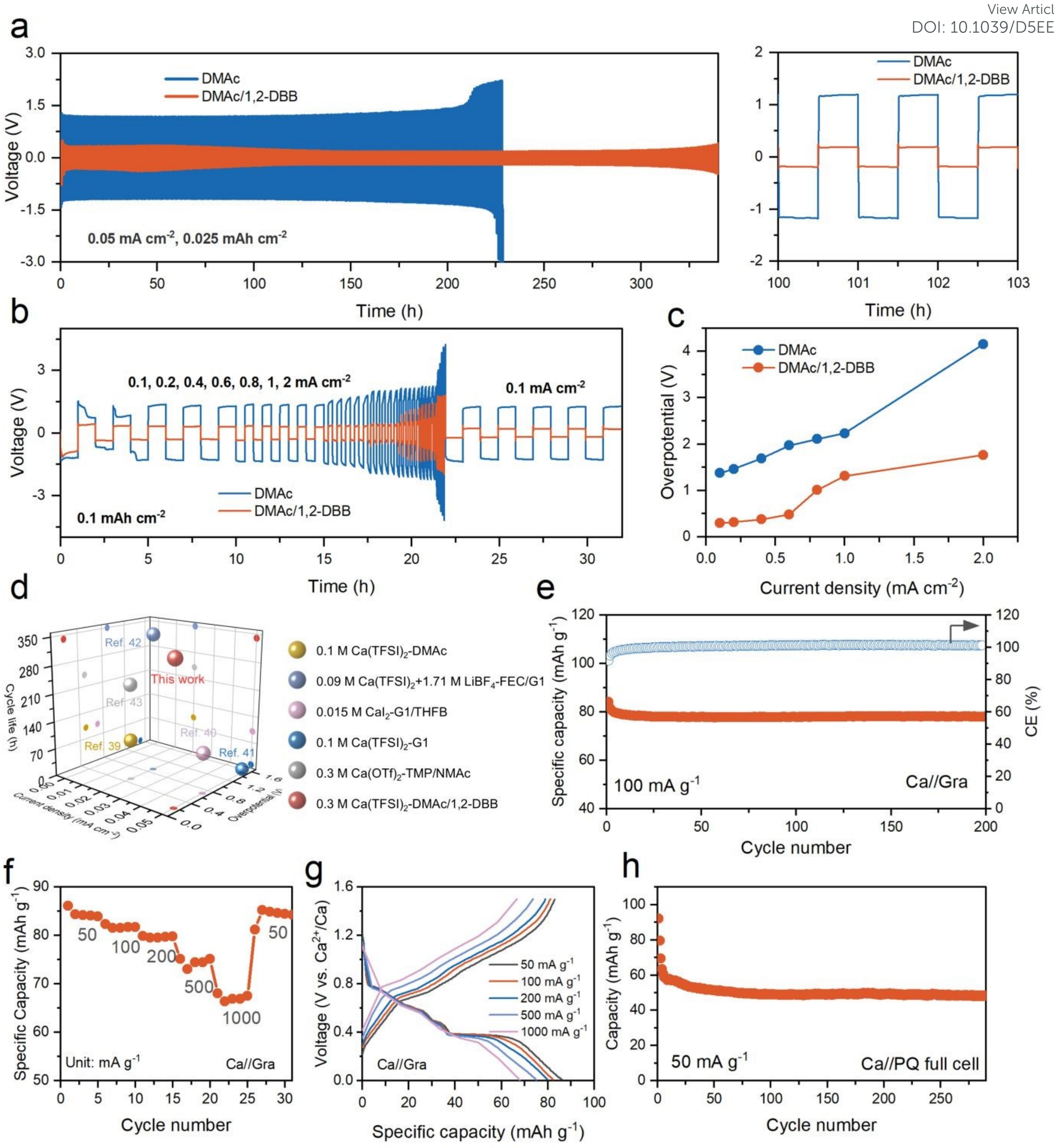

Figure 5. (a) Cycling performance of Ca//Ca symmetric cells in DMAc and DMAc/1,2-DBB electrolytes at 0.05 mA cm^{-2} and 0.025 mAh cm^{-2}. (b) Rate performance of Ca//Ca symmetric cells in DMAc and DMAc/1,2-DBB electrolytes at a constant capacity of 0.1 mAh cm^{-2}. (c) Overpotentials of Ca//Ca cells at increasing current rates derived from (b). (d) Comparison of the electrochemical performance of Ca//Ca symmetric cells in recently reported electrolytes [39-43]. (e) Cycling performance, (f) rate performance and (h) charge-discharge curves of the Ca//Gra cell in the DMAc/1,2-DBB electrolyte. (i) Cycling performance of the Ca//PQ full cell in the DMAc/1,2-DBB electrolyte.

View Article Online
DOI: 10.1039/D5EE07317K

Data Availability Statement

The data supporting this article have been included as part of the Supplementary Information.